Arthropod Structure & Development 46 (2017) 30–38

Contents lists available at ScienceDirect

Arthropod Structure & Development

journal homepage: www.elsevier.com/locate/asd

Nano-channels in the spider fang for the transport of Zn ions to cross-link His-rich proteins pre-deposited in the cuticle matrix

Yael Politi [a, *], Eckhard Pippel [b], Ana C.J. Licuco-Massouh [a], Luca Bertinetti [a], Horst Blumtritt [b], Friedrich G. Barth [c], Peter Fratzl [a]

[a] Department of Biomaterials, Max Planck Institute of Colloids and Interfaces, 14424, Potsdam, Germany
[b] Max Planck Institute of Microstructure Physics, D-06120, Halle/Saale, Germany
[c] Department of Neurobiology, Life Sciences, University of Vienna, Vienna, Austria

ARTICLE INFO

Article history:
Received 29 March 2016
Accepted 7 June 2016
Available online 7 September 2016

Keywords:
Biomaterials
Spider fang
Metal ion coordination
XAS
EELS

ABSTRACT

We identify the presence of multiple vascular channels within the spider fang. These channels seem to serve the transport of zinc to the tip of the fang to cross-link the protein matrix by binding to histidine residues. According to amino acid and elemental analysis of fangs extracted shortly after ecdysis, His-rich proteins are deposited before Zn is incorporated into the cuticle. Microscopic and spectroscopic investigations in the electron microscope and synchrotron radiation experiments suggest that Zn ions are transported through these channels in a liable (yet unidentified) form, and then form stable complexes upon His binding. The resulting cross-linking through the Zn–His complexes is conferring hardness to the fang. Our observations of nano-channels serving the Zn-transport within the His-rich protein matrix of the fibre reinforced spider fang may also support recent bio-inspired attempts to design artificial polymeric vascular materials for self-healing and in-situ curing.

1. Introduction

Spider fangs are mainly used as injection needles to puncture the prey's cuticle and to inject venom. As shown for the wandering spider *Cupiennius salei* (Ctenidae), they are made of a specialised cuticle characterized by macro- and micro-structural gradients as well as compositional gradients along their length and within their tips (Bar-On et al., 2014; Erko et al., 2013; Politi et al., 2012). Specifically, high levels of zinc (Zn), chloride (Cl) and calcium (Ca) are found in the tip and the outermost layer of the fang. Previously, the presence of zinc oxide (ZnO) granules was reported (Politi et al., 2012; Tao et al., 2007). However, the biological relevance of the mineral was questioned (Politi et al., 2012). The material's local mechanical properties, specifically, its hardness and stiffness, as measured by nano-indentation on dry samples, were reported to increase in correlation with increased Zn concentration (Politi et al., 2012). As the histidine (His) residue concentration in the protein matrix also increases from base to tip (where it comprises 25% of the total protein matrix), it was suggested that the material's mechanical enhancement stems from metal ion cross-linking of the protein matrix (Politi et al., 2012). Similar Zn–His interactions, with similar effect on the mechanical properties were reported earlier for annelid jaws (*Nereis virens*) with evidence from extended x-ray absorption fine structure (EXAFS) analysis for the occurrence of a $Zn(His)_3Cl$ complex (Lichtenegger et al., 2003).

Metal ion incorporation at the tips and edges of cuticular structures such as claws, teeth and fangs is common in many arthropods (Degtyar et al., 2014; Schofield, 2003), but little is yet known about the chemical nature and the mechanisms of this incorporation. Schofield et al. (Schofield, 2003) showed the presence of a nano-channel array in Zn-rich cuticular structures in ants (*Tapinoma sessile*) and scorpions (*Vaejovis spinigeris*). In both cases these channels were absent from regions that do not incorporate zinc. The time course of Zn and Cl incorporation into these cuticular regions was then determined by quasi-time dependent x-ray fluorescence (XRF) analysis of the cuticle at different stages after ecdysis. Zn was incorporated many hours after the cuticle in these regions had been fully tanned, suggesting an already heavily cross-linked material. Therefore the distance between the channels was thought to be determined by the distance available for the diffusion of Zn through the tanned matrix (Schofield, 2003).

* Corresponding author. Max Planck Institute of Colloids and Interfaces, Department of Biomaterials, Am Mühlenberg 1, 14424, Potsdam, Germany. Tel.: +49 331 5679463.
E-mail address: yael.politi@mpikg.mpg.de (Y. Politi).

http://dx.doi.org/10.1016/j.asd.2016.06.001

Despite the abundance of His residues in the protein matrix of the spider fang tip, to date there is yet no direct evidence for His–Zn binding in arthropod cuticles and it is unknown at which stage of cuticle formation these interactions take place. In order to gain insight into these questions we used high-resolution transmission electron microscopy (HR-TEM), spectroscopic methods and amino-acid analysis of the adult spider fangs as well as of spiders shortly after ecdysis (the shedding of the old cuticle during moulting) when the spiders were still hanging from their exuviae. Here we present evidence for Zn–His coordination in the mature cuticle protein matrix. Amino-acid analysis revealed that His-rich proteins are deposited before the incorporation of Zn into the cuticle. They are already present in spiders shortly after ecdysis, whereas at this stage Zn is not yet present in the cuticle as determined by elemental analysis. In addition, we show the presence of multiple nano-channels, similar to those observed in ants and scorpions, which after ecdysis are filled with Zn in a labile chemical state readily forming ZnO.

2. Materials and methods

2.1. Samples

Adult specimens of the Central American wandering spider *C. salei* were obtained from the breeding stock of the Department of Neurobiology of the University of Vienna. All experiments were performed according to Germany's animal protection act §8a(4).

2.2. Ecdysis spiders

Spiders were also collected shortly after ecdysis. The exact time is hard to determine, however we chose spiders in which most of the cuticle was still un-tanned.

Poly-L-histidine (Sigma-Aldrich, mol.wt. 5000–25,000, CAS # 26062-48-6) was suspended in water, the pH was lowered using 0.1 M HCl solution until dissolution (pH ~2). For the preparation of PolyHis-Zn, 0.37 equivalents in Zn of a 0.01 M zinc chloride solution (Sigma-Aldrich, ≥98% reagent grade, CAS # 7646-85-7) were mixed. The solutions were precipitated by gradual addition of 0.1 M NaOH solution. The precipitates were washed dried and pressed into a pellet using a hydraulic press (Atlas Series Laboratory 15T hydraulic press). Insulin, chitin and bovine serum albumin (BSA) were purchased from Sigma Aldrich, CAS 9048-46-8.

2.3. Focused ion beam (FIB) lamella preparation

The FIB preparation of the TEM lamellae followed a modified lift-out procedure using low ion beam currents to avoid strong charging and thermal damage of the lamellae. For the perpendicular cross section the first 10 μm of the fang tip were milled-off slice-by-slice; then a 4 μm thick disk was cut off, lifted up by a micromanipulator and glued onto a special TEM grid, where a $10 \times 30\ \mu m^2$ part was thinned to about 0.4 μm in thickness (FIB-1). The freshly milled cross section of the remaining fang tip served as starting plane to produce a second lamella (FIB-2) oriented nearly in parallel to the fang's long axis. About one third of the sample was thinned to a minimum thickness of about 60 nm.

2.4. High Resolution Transmission Electron Microscopy (HR-TEM)

Fang microtome slices (Fang-1, -2,-3) and the FIB samples were viewed with a HR-TEM and in the high angle annular dark field scanning transmission mode (HAADF-STEM), using a FEI TITAN 80-300 electron microscope containing a monochromator and spherical aberration correction. The microscope was operated with an accelerating voltage of 300 kV. The beam convergence was 24 mrad. The inner cut-off for the dark field detector was about 50 mrad and the estimated probe current was 0.8 nA.

Electron energy loss spectroscopy (EELS) measurements were performed with a Gatan GIF 866 TRIDIEM ERS electron energy loss spectrometer. Background removal and normalization were achieved using the EELS module of the Digital-micrograph (Gatan 1.7.1) software. Acquisition time of each EELS spectrum was about 1 s. The electron dose (fluence) was estimated up to 100 nA/nm^2. A monochromator was used for HR-EELS spectra. 3–7 spectra/sample from different positions were averaged.

2.5. Energy-dispersive X-ray spectroscopy (EDX) mapping in TEM

EDAX detector and a digital pulse processor were used. Acquisition time for each EDX point identification was about 1 s, and about 5 min for mapping.

2.6. EDX mapping in SEM

EDX measurements were performed using a JEOL JSM-7500F scanning electron microscope equipped with two Oxford Instruments Ltd. X-max 150 silicon drift detectors. The simultaneous acquisition of the spectra through the dual system was controlled using the AZtec energy suite (Oxford Instruments Ltd.). Accelerating voltage was set to 20 kV, and the beam current optimized to achieve an input count rate of around 40 k count s^{-1}. A minimum of $2.5^* \times 10^6$ counts were accumulated per spectrum. For the semi-quantitative analysis the EDS spectra were processed with the quantification tool of the AZtec energy suite using the internal standards included in the software. For every sample 3 different areas were studied.

Importantly, the samples measured at the SEM are the same samples that were analysed for their amino-acid content.

2.7. X-ray absorption spectroscopy (XAS)

Frozen fang samples and insulin were kept at −60 °C throughout the measurement. PolyHis-Zn powder sample was mounted on a carbon sticky tape, and ZnCl2 solution was mounted between Kapton films with a 0.5 mm spacer. Data were collected at the Bessy II synchrotron (HBZ Berlin) at the KMC-2 beamline. The samples were measured in fluorescence geometry using an energy dispersive detector. Beamline KMC-2 operates on a bending magnet and the beam energy is defined by a Si (111) monochromator. High-order harmonics are removed by harmonic rejection mirrors upstream of the monochromator. The beam size at the sample was about $0.5 \times 0.5\ mm^2$. XAS spectra were scanned from −150 eV to +800 eV from the edge (E = 9659 eV). Energy calibration used the measurement of a sample of metallic zinc. For each sample 3–4 spectra were averaged. Data processing and normalization were performed using the Demeter data analysis package (Ravel and Newville, 2005).

2.8. Amino acid analysis

The amino acid composition of 2 segments of 3 fangs were determined by Genaxxon bioscience GmbH using amino Acid Analyser LC3000. Each sample was supplemented with HCl (600 μL 6 N), sealed under vacuum (<20 mbar) and hydrolyzed for 96 h at 110 °C. After hydrolysis, samples were dried at 36 °C for 4 h (vacuum centrifuge). Each dried sample was supplemented with Na-Acetat buffer (500 μL, pH = 2.2) for subsequent derivatization

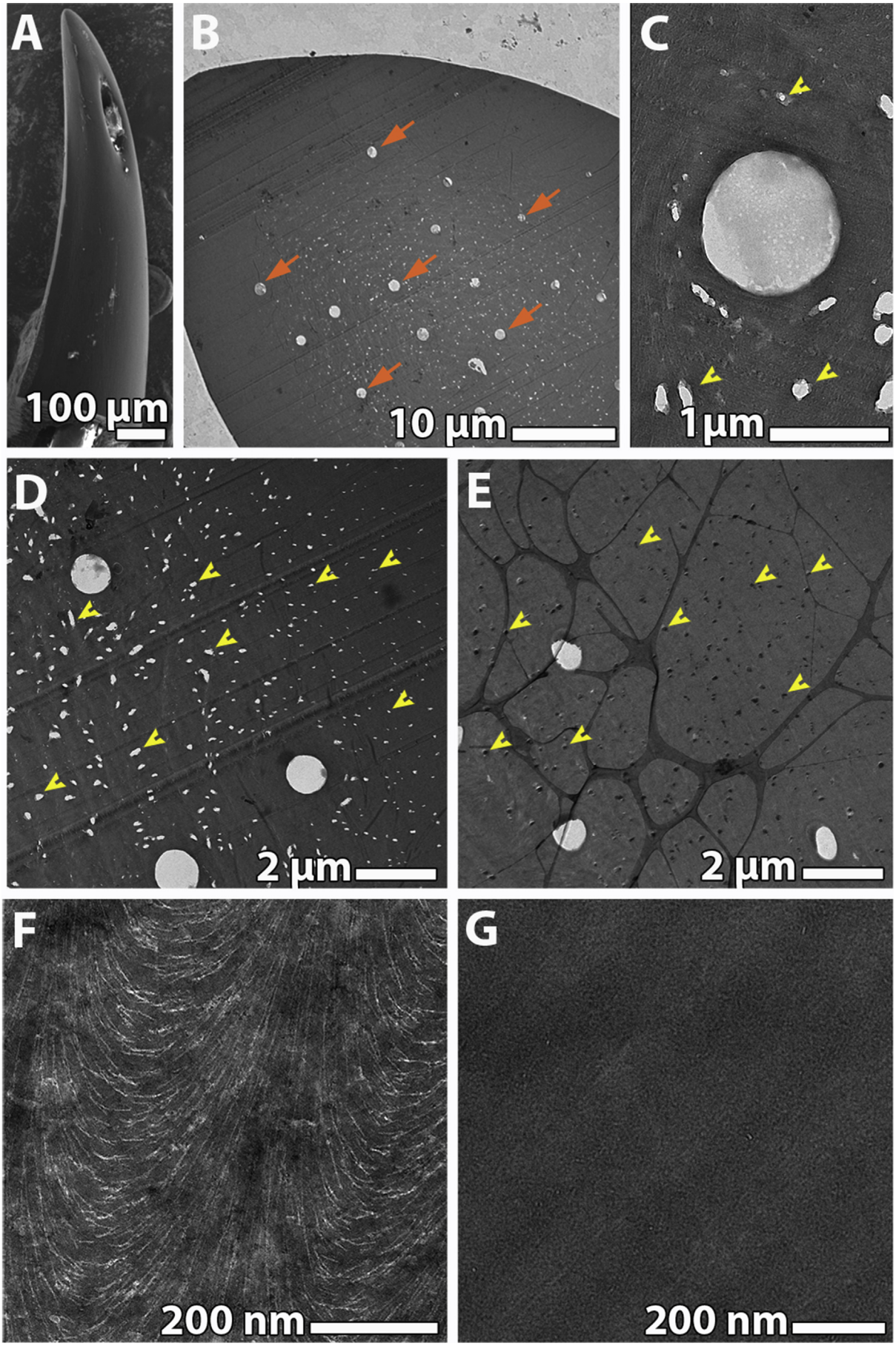
A
100 µm
B
10 µm
C
1 µm
D
2 µm
E
2 µm
F
200 nm
G
200 nm

and high-pressure liquid chromatography (HPLC; polymeric cation exchange column). Fragmented amino acids were detected by post-column Ninhydrin derivatisation at 125 °C and photometric measurement at 570 nm. Data was monitored by the chromatography software ChromStar 6.0. Following calibration of the HPLC using a commercial standard (Sigma-Aldrich, A2908).

3. Results

3.1. Nano-channel structure and contents

The spider fang is a curved conical and hollow injection needle, with the opening of the venom canal close to its tip (Fig. 1A). Using electron microscopy we investigated fang samples, which were either taken from spiders shortly after ecdysis or from mature adult spiders. The fangs were either dissected from the spider immediately before analysis or several weeks before and stored in ethanol. In unstained sections taken from the tip (around 2–5 μm below the tip) of the fang of adult spiders (fresh samples) a number of canals with circular cross-section can be seen (Fig. 1B, C). In addition there are numerous smaller, irregularly shaped pores in freshly prepared samples (Fig. 1C, D). We refer to these from now on as nano-channels. In TEM images of unstained *ethanol-stored* slices taken from similar positions, i.e. the tip of the fang of adult spiders, objects with similar shape and size are observed, but here they show high electron density (Fig. 1E) and their content is identified as ZnO by selected-area electron diffraction (SAED) (Fig. S-1). Thus, the content of the nano-channels is not found in fresh samples, suggesting that it had either dissolved or detached from the fresh fang during sample preparation, which involves floating the thin sections in a water bath. In adult spiders, Zn also occurs in the protein matrix. Therefore, in both fresh and ethanol-stored samples, the matrix shows high mass-thickness contrast relative to the chitin-protein fibres, which makes the fibres visible even without staining the sample (Fig. 1F). In the regions below the venom canal opening, where Zn is absent (Fig. 1G), the mass-thickness contrast does not suffice to resolve the chitin-protein fibres in the protein matrix.

In fang samples severed from spiders shortly after ecdysis similar circular cross-section canals and nano-channels are found. However, using EDX and EELS in these samples we found no Zn incorporation in either the matrix or the nano-channels (Fig. S-5).

To minimize the sample exposure to external water, ethanol or air, which could dissolve the labile Zn-rich phase or induce the formation of ZnO, Focused Ion Beam (FIB) lamellae (sections) were prepared from fresh fangs (at inter-moult stage) previously freeze dried and stored under argon atmosphere. The first slice (FIB-1) was cut 12 μm from the tip, perpendicular to the long axis of the fang (Fig. 2A). A second slice (FIB-2) was cut out just below slice FIB-1 and oriented orthogonally to it (that is roughly parallel to the fang long axis) (Fig. 2B). When using high-angle annular dark-field imaging scanning transmission electron microscopy (HAADF-STEM), the protein matrix appears bright, indicating the incorporation of heavy elements, whereas the chitin-protein fibres appear dark (Fig. S-2). Energy dispersive x-ray (EDX) analysis confirms the presence of Zn and Cl in the protein matrix (Fig. S-4). Bright contrast in STEM mode was also observed within numerous nano-channels measuring 50–200 nm in width (Fig. 2C–F). At low magnifications we observed distinct regions with a high density of nano-channels in the centre of the fang (centre of FIB-section) and in the periphery (Fig. S-3). The channels appear to run in a helicoidal trajectory and roughly parallel to the fang long axis (i.e. perpendicular to the section surface) (Fig. 2C, S-3C). This is seen more clearly when changing the depth of focus to about 100 nm for section FIB-1, which is about 400 nm thick (see Section 2). Such trajectory is common for channels (e.g., pore-canals) that run orthogonally to the orientation of the fibre lamellae in various plywood structures (Barth, 1970; Locke, 1961). Close to the fang periphery, longer stretches of the nano-channels are clearly visualised as wavy structures within the focus field suggesting that here the channels turn and run in a direction more parallel to the surface of the slice (i.e. perpendicular to the fang surface) (Fig. 2D). In order to better understand the morphology of the channels and for spectroscopic analyses of the content of both the matrix and channels, we examined the second FIB section (FIB-2), in which one edge was thinned to 60 nm. Section FIB-2 was cut perpendicular to FIB-1 and parallel to the long axis of the fang (Fig. 2B). In this view, the long channels are seen running parallel to the slice surface and the walls of the channels are decorated by ~5 nm ZnO nanoparticles (Fig. 2E, F).

EDX mapping of the FIB-2 sample (Fig. 3) shows that the concentrations of Zn, Cl and O are higher in the channel than in the surrounding protein matrix, whereas the N concentrations are the same. Following EDX mapping and local measurements ('point identification') even in freeze-dried samples ZnO nano-particles can be found within larger nano-channels (width larger than 50 nm). The Zn/O ratio varies considerably in the smaller channels close to the fang periphery. Thus we conclude that a large fraction of the Zn ions in the channels is precipitated to form ZnO in freeze-dried and in ethanol-stored specimens, likely due to drying, which increases the local Zn concentration.

3.2. Matrix amino acid composition shortly after ecdysis

We analysed the amino acid composition of fangs extracted from spiders shortly after ecdysis comparing the amino acid distribution at the tip and at the base of the fangs. The results (Fig. 4, Table S-1) show that His is already enriched in the tip of the fang relative to its base at this stage. In fact, the matrix composition is very similar to the matrix composition reported before (Politi et al., 2012) for adult spider fangs (long after moulting).

3.3. Zn–His coordination

Since Zn is known to coordinate histidine in other organisms (Degtyar et al., 2014; Schmitt et al., 2015), we performed Nitrogen K-edge electron energy loss spectroscopy (EELS) and Zn K-edge X-ray absorption spectroscopy (XAS) to test the possibility of Zn–His coordination in the spider fang. Core-level spectroscopy such as XAS and EELS are sensitive techniques to study the chemical environment around a selected element of interest. Nitrogen K-edge EELS analysis was chosen to allow insight into the chemistry of the protein-matrix, while exploiting the high lateral resolution

Fig. 1. Electron micrographs of the spider's fang. (A) SEM image showing the distal part of the spider fang. (B) TEM micrograph overview of freshly prepared fang sections showing numerous canals about 1 μm in diameter (arrows) and multiple irregular nano-channels (seen as small white spots). (C) High magnification of one of the large canals and the nano-channels (a number of nano-channels are marked with yellow arrow-heads). (D) TEM micrograph of freshly cut microtome section showing the circular cross-section canals and a multitude of irregular nano-channels (arrow-heads). Note microtome knife marks as diagonal lines across the image. (E) Ethanol stored material; microtome section showing canals, and a multitude of highly dense particles (arrow-heads). The carbon film support appears as a dark continuous lacy film. (F) High magnification of the cuticle at the tip of the fang, showing typical appearance of fibres in the plywood arrangement, which appear bright relative to the Zn enriched protein matrix. (G) High magnification of the fang cuticle in a section cut below the opening of the venom canal, a region without Zn incorporation. The mass density contrast between the fibres and the matrix is insufficient to distinguish between them.

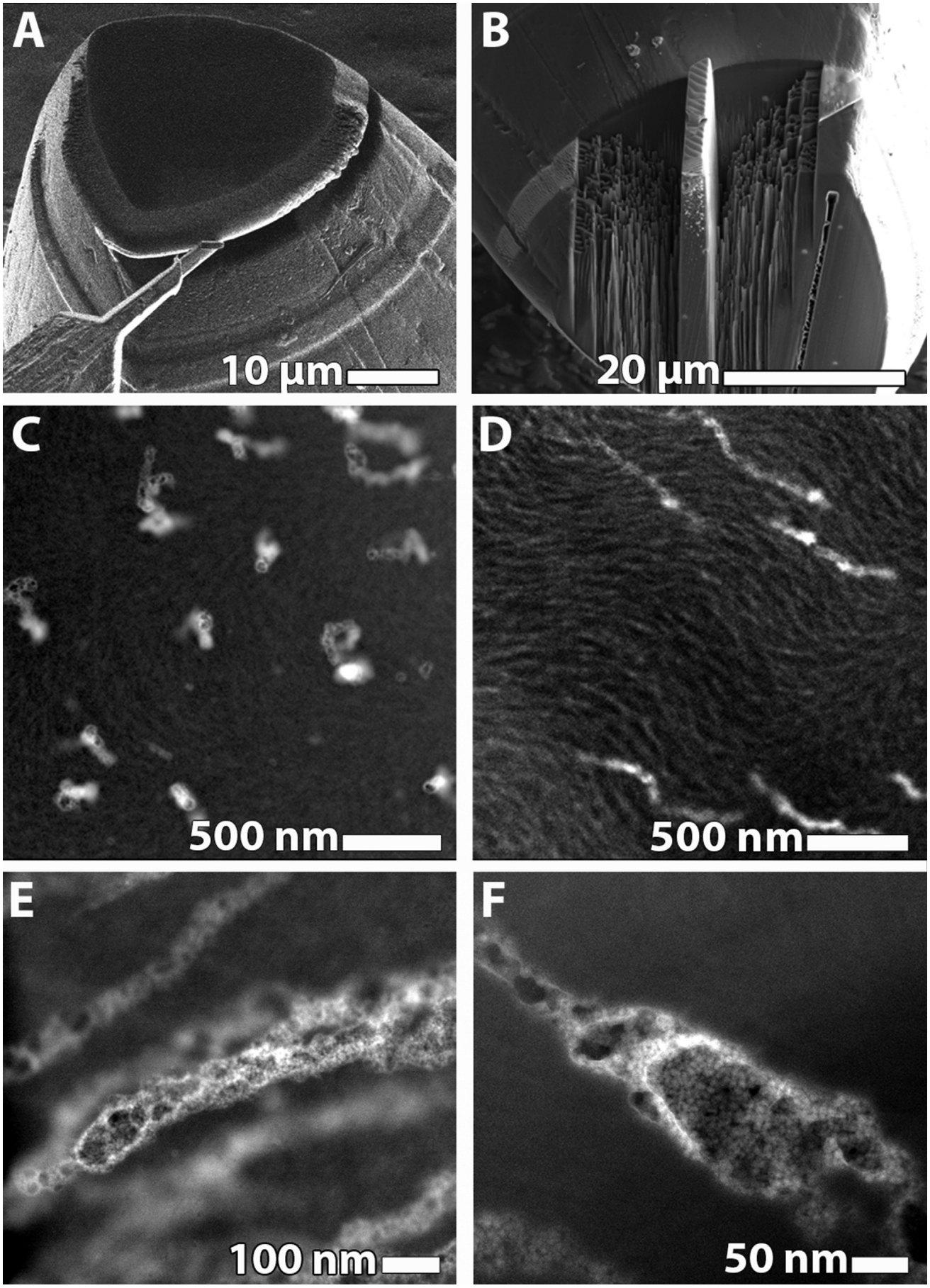
A
10 µm
B
20 µm
C
500 nm
D
500 nm
E
100 nm
F
50 nm

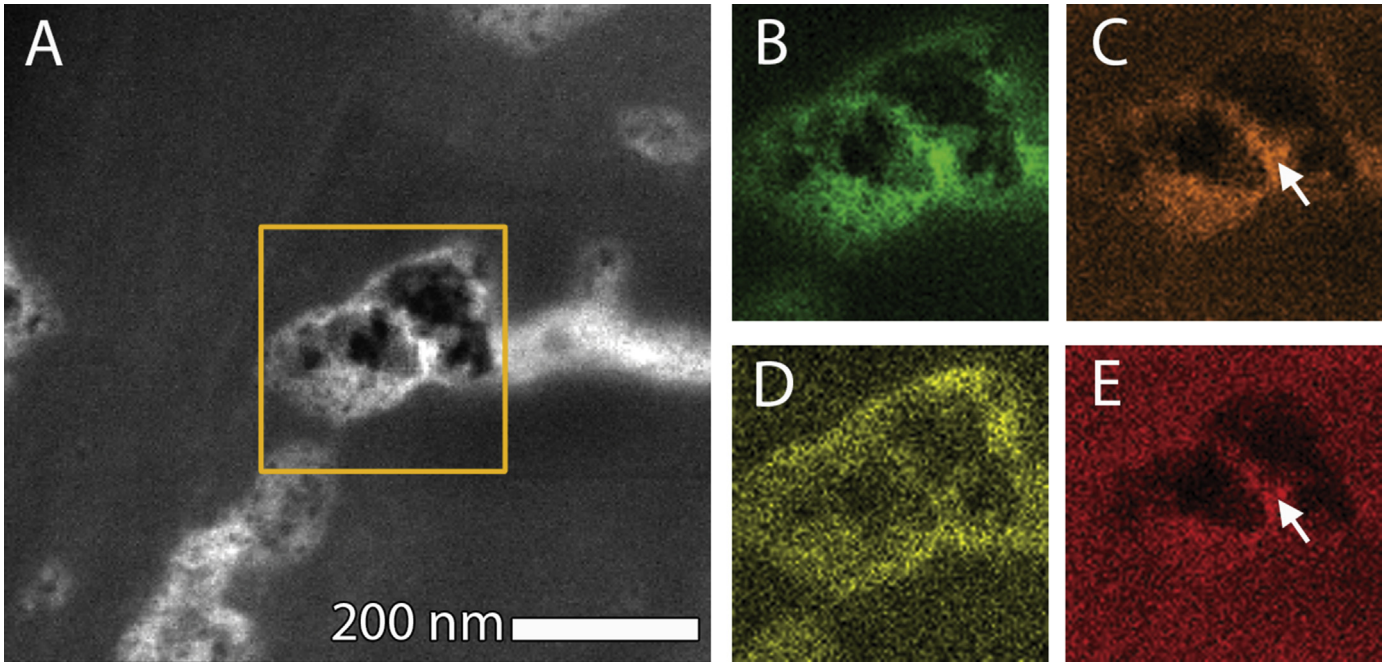

Fig. 3. EDS Mapping of one of the nano-channels in FIB-2. (A) HAADF image of the channels. The square shows where the mapping was performed. (B) Zn distribution, (C) oxygen, (D) chlorine and (E) nitrogen. The arrows in (C) and (E) show a region where the apparent increase in N concentration results from an actual increase in O concentration. The higher O signal introduces an increased background for the N signal.

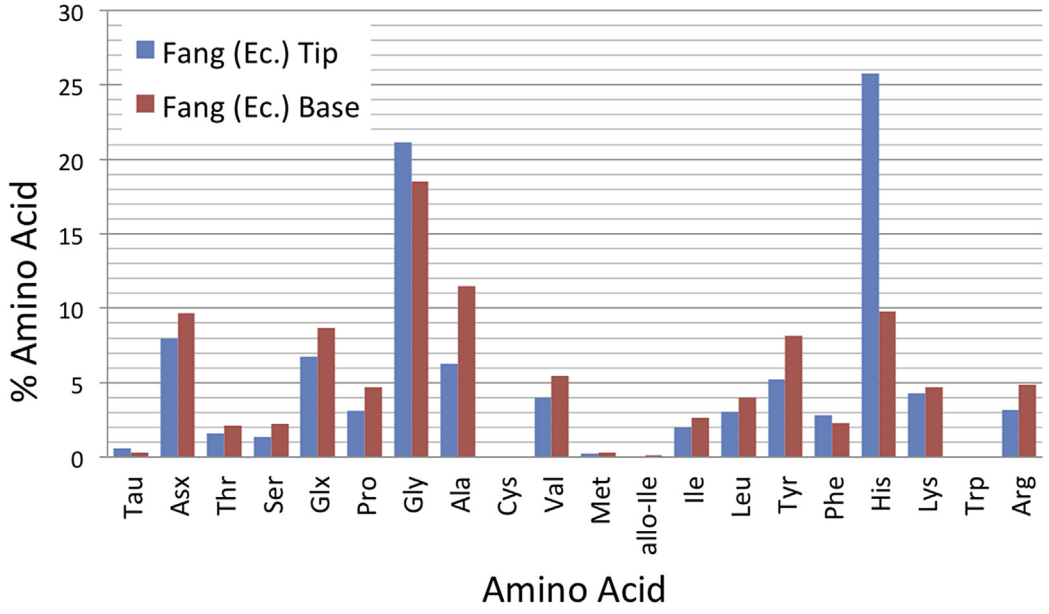

Fig. 4. Amino acid analysis of fangs extracted from spiders right after ecdysis. A comparison between the tip and the base of 6 fangs.

of the TEM (in the order of 0.5 nm in the present case) to investigate the matrix without contribution from the contents of the nano-channels. We analysed the fang matrix above the opening of the venom canal (Fang-1, Fang-2), where Zn is abundant, and close to it (Fang-3), where Zn concentration is considerably lower (Table S-2). In addition we used N K-Edge EELS to study the matrix in fangs extracted immediately after ecdysis (Fang – Ec.) where we found no traces of Zn incorporation. In all the fang samples,

Fig. 2. Focused Ion Beam (FIB) lamella prepared from a freeze-dried fang. (A) SEM image showing the lifting of the slice (FIB-1). (B) Preparation of second FIB section (FIB-2) cut perpendicular to the first section. (C–D) HAADF micrographs (Z contrast, brighter shade corresponds here to higher Zn content) of FIB-1 showing the Zn rich matrix (bright contrast) and elongated nano-channels with increased Zn concentration. (C) High magnification at the centre fang showing the helicoidally trajectory of the nano-channels. Only parts of the channels are "in focus" due to the large thickness of the slice (400 nm). (D) at the edges large portion of the channels are in the focus plane. (E) HAADF image of the second FIB section (FIB-2). (F) High magnification HAADF image of one nano-channel showing multiple ZnO nanoparticles of about 5 nm in diameter decorating the inner surface of the channel.

the spectra contain contributions from all nitrogen containing molecules – including chitin and proteins. However, His residues comprise around 25% of the total amino acid composition of the protein matrix at the tip of the fang in both adult spiders and in fangs of spiders right after ecdysis. We compared the EELS spectra of the fang to a series of commercially available controls poly-histidine (PolyHis), chitin and bovine serum albumin (BSA), a protein that contains a relatively small amount of histidine as a reference for protein main-chain contribution. In addition, poly-histidine peptides were complexed with Zn (PolyHis-Zn) and measured under the same conditions. The spectra (Fig. 5) received have similar line shapes and vary only little in peak position. The main observation, however, is the increase in the intensity of the π^* peak relative to the σ^* peak (originating from $1s \rightarrow \pi^*$ and $1s \rightarrow \sigma^*$ electronic transitions, respectively) in samples enriched with Zn. This can be seen both in the synthetic model PolyHis-Zn (Fig. 5A) and in the fang (Fig. 5B). It is important to note that other factors may also affect the fang spectra such as variations in the cuticle composition (specific amino acid composition and chitin to protein ratios) and the orientation of the chitin-protein fibres or of the His ring. The change in peak ratio is observed in both powder samples (PolyHis and PolyHis-Zn) and in two orthogonal fang sections (specifically, section "Fang-1" and FIB-2). We therefore conclude that effects due to sample orientation are not modifying the observation that Zn complexation leads to an increase in the intensity of the π^* peak. High-energy resolution scans using a monochromator, which also reduces the electron flux (see Section 2), confirmed the variation in peak intensity excluding radiation damage artefacts (Fig. 5C). These high-resolution spectra provide additional information about the binding. The N K-edge XAS spectrum of His reported before (Zubavichus et al., 2005) shows two well-defined π^* peaks of similar intensity (at 400 and 401.6 eV), which were assigned to the two nitrogen atoms in the heterocyclic imidazole ring (the Nδ1 and Nε2, respectively). The corresponding peak for the amide bond ($N_{C=O}$) occurs around 401.4 eV, that is, very close to one of the imidazole peaks (Apen et al., 1993; Feyer et al., 2010; Leinweber et al., 2007; Zubavichus et al., 2005) (a schematic of PolyHis is illustrated in Fig. S-6). Thus, in PolyHis the π^* peak at higher energy contains contributions from both components: the amide nitrogen ($N_{C=O}$), and Nε2 (Leinweber et al., 2007). Upon Zn binding via Nδ1, the low energy π^* peak shifts to higher energy because the electron lone pair of the imino nitrogen is now involved in Zn binding and the effective nuclear charge is increased. This shift results in the increased intensity of the higher energy π^* peak, which now contains contributions from three nitrogen species: $N_{\varepsilon 2}$, $N_{\delta 1}$-Zn and $N_{C=O}$. Similar observations have been reported for histidine containing peptides adsorbed on gold surfaces (Feyer et al., 2010). H-bonding in PolyHis will cause an energy shift in peak position the same direction, but to a lesser extent (Apen et al., 1993). Due to the low concentration of nitrogen in the nano-channels we could not perform EELS spectroscopy there. Table S-2 of the supporting information summarizes the relationships between EELS data and elemental composition for each spectrum.

The occurrence of His-Zn cross-links in the protein matrix is strongly supported by the nitrogen K-edge EELS data. We performed also Zn K-edge XAS measurements on whole fang samples, using an x-ray beam of about 200 × 500 μm^2. A comparison of the x-ray absorption near edge structure (XANES) line-shape of the fang (freshly severed from the animal, rapidly frozen in liquid nitrogen and measured at −60 °C) to insulin, PolyHis-Zn and Zn in solution (0.5 M $ZnCl_2$, at room temp.) is presented in Fig. 6. The intensity of the main peak in the fang spectrum reaches ~1.4 (normalized intensity). This is intermediate between that of insulin or polyHis-Zn (~1.3), and that of Zn frozen solution (~1.5). The intensity of the main absorption peak in Zn K-edge XAS spectra is known to relate to the coordination number where in octahedral coordination the peak is ≥1.5, and in tetrahedral it is <1.5 (Frankær et al., 2012). By comparison to insulin, known to coordinate 3 His and 1 Cl in a tetrahedral coordination, we can also deduce a tetrahedral coordination for PolyHis-Zn. In aqueous solution of $ZnCl_2$, the Zn ion resides in an octahedral coordination with 6 water molecules (Ohtaki and Radnai, 1993; Pavlov et al., 1998). Notable also is a double peak line-shape at the near edge region (E = 9665–9670 eV) in both the insulin and PolyHis-Zn sample, but missing or broadened in the fang and $ZnCl_2$ spectra. The line shape of the fang spectrum lacks these clear features; however, it resembles the spectrum of octahedral coordinated Zn in T6 insulin (Frankær et al., 2012) and a similar line shape was reported for His_x/Asp_x-Zn coordination in mussel byssus threads (Schmitt et al., 2015). We emphasize that the fang XANES spectrum represents

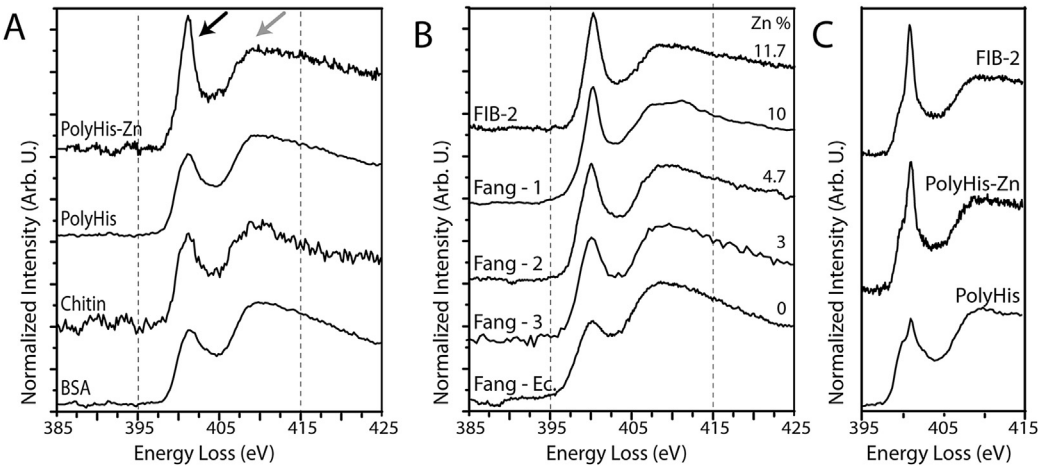

Fig. 5. (A) N K-edge EELS spectra of the selected controls. The π^* peak is denoted by a black arrow, the σ^*-peak by a grey arrow. The dashed lines indicate the energy range used in (C) for the high energy resolution spectra. (B) N K-edge EELS spectra of the spider fang. The relative atomic percent of Zn present in the sample is indicated for each spectrum. Note that FIB-2 and fang-1 have similar Zn content and originate from similar position on the fang; however, they are orthogonal to each other. FIB-2 is cut parallel to the fang long axis, and fang-1 is cut perpendicular to it. (C) High energy resolution spectra taken using a monochromator.

an average spectrum of Zn in the nano-channels and in the protein matrix.

4. Discussion

Using high resolution TEM we identify two major pools of Zn in the tip of the spider fang, the protein matrix and Zn-rich nano-channels. According to element specific (Zn, N) spectroscopic (XAS and EELS) analyses Zn is bound to the protein matrix at least in part via histidine residues which are abundant in the protein matrix of the fang tip. Elemental and amino acid analysis of fangs from ecdysing spiders show that Zn is incorporated into the fang tip only some time after ecdysis, whereas histidine is already present in the matrix at this stage. Thus, the nano-channels likely function to transport the Zn ions into the pre-deposited, already partly tanned matrix. There they bind and cross-link the histidine residues.

4.1. His–Zn binding in the protein matrix

The occurrence of Zn and histidine in the tip of the spider fang was suggested to contribute to the increased indentation hardness and stiffness of the fang tip reported before (Politi et al., 2012). The notion of a biological function of metal-ion cross-linking in the hardening of tips and edges of specialized tools has been suggested before. EDTA treated samples of the jaws of the annelid *N. virens*, in which a large part of Zn ions is removed, showed a drastic reduction in hardness and stiffness measured by nano-indentation, while re-introduction of the Zn or other transition metals recovered their original properties to a large extent (Broomell et al., 2008, 2006).

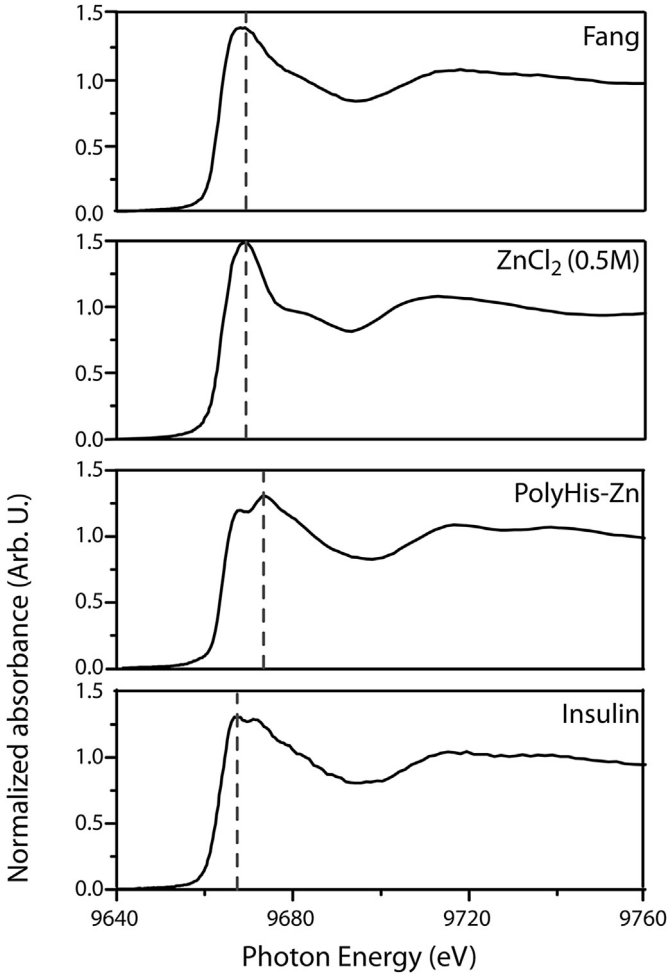

Fig. 6. Zn K-edge XANES spectra of the Fang, PolyHis-Zn, Insulin and 0.5 M $ZnCl_2$ solution. The dashed line indicates the position of the most intense peak of insulin, PolyHis-Zn and $ZnCl_2$ (sol).

The incorporation of His rich proteins occurs before the incorporation of Zn as determined by the amino acid analysis of fangs from ecdysing spiders. So far, however, we do not know whether they are introduced before or during the pre-ecdysal tanning. Chitin–binding proteins in stiff insect cuticles often contain an increased number of His residues (the so-called "extended R&R consensus sequence" – a common amino acid sequence found in chitin-binding proteins in many arthropod groups) relative to chitin-binding proteins from soft cuticular regions (Iconomidou et al., 2005). These His residues were predicted by molecular modelling to face away from the chitin binding cleft allowing the formation of intermolecular cross links with other matrix components (Iconomidou et al., 2005). However, these alone cannot account for the large proportion of histidine in the matrix (25%). It is possible that the His-rich proteins comprise another family of matrix proteins. For example, RNA-sequencing and proteomic studies of the protein matrix of the squid beak revealed two protein families: chitin-binding proteins which are initially deposited and connect the chitin chains, and a His-rich modular protein family which is secreted later and infiltrates the chitin-protein scaffold (Tan et al., 2015). In the squid beak, His residues cross-link with other amino-acid residues and Zn is absent from this system (Miserez et al., 2008). In the spider fangs, the histidine rich proteins are pre-deposited in the matrix and are cross-linked at a later stage by Zn ions.

4.2. Nano-channels

Sample preparation for TEM involves floating the newly sectioned slices on water before mounting them on the TEM grid. This stage may remove soluble components from the sample (Seto et al., 2012). When a fresh fang sample is viewed in the transmission electron microscope, the channels appear as holes in the slice, indicating that the content of the channels in fresh fangs is water-soluble. If the sample is dried before slicing, Zn precipitates in the channels in the form of ZnO and, since this mineral is less soluble, it remains after cutting. The Zn content in the matrix, on the other hand, is not affected by the water treatment. Thus, the Zn concentrated in the multitude of nano-channels resides in a soluble chemical state and highly concentrated (with a tendency to convert to ZnO upon dehydration). Estimated from the volume fraction of the ZnO precipitate in the channels, the initial Zn concentration in the channels might be in the molar range (see supporting information). This is striking since the solubilities of $Zn(OH)_2$ and ZnO are orders of magnitude lower (Govender et al., 2004) at biologically relevant pH values (the solubility product, *Ksp*, of both is in the order of 10^{-17}). This means that Zn can be transported either by complexation (i.e. with transport protein) or by keeping the pH within the channels low. At the moment we cannot determine what is the specific Zn coordination in the channels.

In addition to the nano-channels, we observed ~1 μm wide large canals running along the long axis of the fang (Fig. 1B, C). These canals are connected to the surface of the fang, differing from the nano-channels, which stop at varying distances from the surface within the depth of the cuticle material. We did not detect a high concentration of Zn within the large canals and do not know whether these two types of channels are connected. Thus the function of the large canals remains unknown at this point. We note that these large canals are different from the pore-canals commonly observed in arthropod cuticles despite

their similar size. Pore-canals originate at the epithelium and extend up to the epicuticle but do not cross it like the large canals observed here.

At the moment we don't know the manner in which Cl and Ca are incorporated in the fangs. At the time of ecdysis Cl ions were present in the matrix in varying amounts (Table S-2) but not in the channels. In adult fangs Cl is present in both matrix and in the channels. This may indicate that also Cl ions occur in at least two different forms; some proteins may be chlorinated and present in the matrix before ecdysis. In addition, Cl ions may bind to Zn ions during transport and take part in Zn coordination in the matrix. This occurs in the *Nereis* jaws, in which tyrosine residues are chlorinated (Birkedal et al., 2006) and Cl is also involved in the Zn coordination forming $Zn(His)_3Cl$ complexes (Lichtenegger et al., 2003). Further research is needed to answer this question.

5. Conclusions

Using EELS spectroscopy we show evidence for Zn-Histidine cross-links in the tip of the spider fang. These cross-links serve to increase the local hardness and stiffness of the fang material (Politi et al., 2012). We find that Zn is incorporated into the matrix after ecdysis, while histidine is already present in the matrix at this stage. HR-TEM shows the presence of a nano-scale vascular array at the tip of the spider fang, which we propose to serve the transport of Zn to the already partly tanned protein matrix. Our results shed new light onto the formation of biological materials cross-linked by metal ions and may support bio-inspired attempts to synthesise metal-coordinated materials and vascular materials (Holten-Andersen et al., 2011; White et al., 2014).

Acknowledgements

The authors thank the Department for Neurobiology of Vienna University for kindly helping with the animal material. We thank Birgit Schonert and Rona Pitschke for help in sample preparation and TEM observation; Dr. Ivo Zizak and Dr. Maria Brzhezinskaya, beamline scientists at KMC2, Bessy II, for help with XAS measurements and HZB for the allocation of synchrotron radiation beamtime.

Appendix A. Supplementary data

Supplementary data related to this article can be found at http://dx.doi.org/10.1016/j.asd.2016.06.001.

References

Apen, E., Hitchcock, A.P., Gland, J.L., 1993. Experimental studies of the core excitation of imidazole, 4,5-dicyanoimidazole, and s-triazine. J. Phys. Chem. 97, 6859–6866. http://dx.doi.org/10.1021/j100128a019.

Bar-On, B., Barth, F.G., Fratzl, P., Politi, Y., 2014. Multiscale structural gradients enhance the biomechanical functionality of the spider fang. Nat. Commun. 5, 3894. http://dx.doi.org/10.1038/ncomms4894.

Barth, F.G., 1970. Die Feinstruktur des Spinneninteguments I. Die räumliche Anordnung der Mikrofasern in der lamelierten Cuticula und ihre Beziehung zur Gestalt der Porenkanäle (*Cupiennius salei* Keys., adult, häutungsfern, Tarsus). Z. Zellforsch 104, 87–106.

Birkedal, H., Khan, R.K., Slack, N., Broomell, C., Lichtenegger, H.C., Zok, F., Stucky, G.D., Waite, J.H., 2006. Halogenated veneers: protein cross-linking and halogenation in the jaws of nereis, a marine polychaete worm. Chembiochem 7, 1392–1399. http://dx.doi.org/10.1002/cbic.200600160.

Broomell, C.C., Mattoni, M.A., Zok, F.W., Waite, J.H., 2006. Critical role of zinc in hardening of Nereis jaws. J. Exp. Biol. 209, 3219–3225. http://dx.doi.org/10.1242/jeb.02373.

Broomell, C.C., Zok, F.W., Waite, J.H., 2008. Role of transition metals in sclerotization of biological tissue. Acta Biomater. 4, 2045–2051. http://dx.doi.org/10.1016/j.actbio.2008.06.017.

Degtyar, E., Harrington, M.J., Politi, Y., Fratzl, P., 2014. The mechanical role of metal ions in biogenic protein-based materials. Angew. Chem. Int. Ed. 53 http://dx.doi.org/10.1002/anie.201404272, 12026–10244.

Erko, M., Hartmann, M.A., Zlotnikov, I., Valverde Serrano, C., Fratzl, P., Politi, Y., 2013. Structural and mechanical properties of the arthropod cuticle: comparison between the fang of the spider Cupiennius salei and the carapace of American lobster Homarus americanus. J. Struct. Biol. 183, 172–179. http://dx.doi.org/10.1016/j.jsb.2013.06.001.

Feyer, V., Plekan, O., Tsud, N., Cháb, V., Matolín, V., Prince, K.C., 2010. Adsorption of histidine and histidine-containing peptides on Au(111). Langmuir 26, 8606–8613. http://dx.doi.org/10.1021/la904684e.

Frankær, C.G., Vad Knudsen, M., Nore'n, K., Nazarenko, E., Stahl, K., Pernille, H., Knudsen, M.V., Norén, K., Ståhl, K., Harris, P., 2012. The structures of T6, T3 R3 and R6 bovine insulin: combining X-ray diffraction and absorption spectro-scopy. Acta Crystallogr. Sect. D. Biol. Crystallogr. D68, 1259–1271. http://dx.doi.org/10.1107/S090744491202625X.

Govender, K., Boyle, D.S., Kenway, P.B., Brien, P.O., 2004. Understanding the factors that govern the deposition and morphology of thin films of ZnO from aqueous solution. J. Mater. Chem. 14, 2575–2591.

Holten-Andersen, N., Harrington, M.J., Birkedal, H., Lee, B.P., Messersmith, P.B., Lee, K.Y.C., Waite, J.H., 2011. pH-induced metal-ligand cross-links inspired by mussel yield self-healing polymer networks with near-covalent elastic moduli. Proc. Natl. Acad. Sci. U.S.A. 108, 2651–2655. http://dx.doi.org/10.1073/pnas.1015862108.

Iconomidou, V.A., Willis, J.H., Hamodrakas, S.J., 2005. Unique features of the structural model of "hard" cuticle proteins: implications for chitin-protein interactions and cross-linking in cuticle. Insect Biochem. Mol. Biol. 35, 553–560. http://dx.doi.org/10.1016/j.ibmb.2005.01.017.

Leinweber, P., Kruse, J., Walley, F.L., Gillespie, A., Eckhardt, K.U., Blyth, R.I.R., Regier, T., 2007. Nitrogen K-edge XANES – an overview of reference compounds used to identify unknown organic nitrogen in environmental samples. J. Synchrotron Radiat. 14, 500–511. http://dx.doi.org/10.1107/S0909049507042513.

Lichtenegger, H.C., Schöberl, T., Ruokolainen, J.T., Cross, J.O., Heald, S.M., Birkedal, H., Waite, J.H., Stucky, G.D., 2003. Zinc and mechanical prowess in the jaws of Nereis, a marine worm. Proc. Natl. Acad. Sci. 100, 9144–9149.

Locke, M., 1961. Pore canals and related structures in insect cuticle. J. Biophys. Biochem. Cytol. 10, 589–618. http://dx.doi.org/10.1083/jcb.10.4.589.

Miserez, A., Schneberk, T., Sun, C., Zok, F.W., Waite, J.H., 2008. The transition from stiff to compliant materials in squid beaks. Science 319, 1816–1819. http://dx.doi.org/10.1126/science.1154117.

Ohtaki, H., Radnai, T., 1993. Structure and dynamics of hydrated ions. Chem. Rev. 93, 1157–1204. http://dx.doi.org/10.1021/cr00019a014.

Pavlov, M., Siegbahn, P.E.M., Sandstro, M., 1998. Hydration of beryllium, magnesium, calcium, and zinc ions using density functional theory. J. Phys. Chem. 5639, 219–228.

Politi, Y., Priewasser, M., Pippel, E., Zaslansky, P., Hartmann, J., Siegel, S., Li, C., Barth, F.G., Fratzl, P., 2012. A Spider's fang: how to design an injection needle using chitin-based composite material. Adv. Funct. Mater 22, 2519–2528. http://dx.doi.org/10.1002/adfm.201200063.

Ravel, B., Newville, M., 2005. ATHENA, ARTEMIS, HEPHAESTUS: data analysis for X-ray absorption spectroscopy using IFEFFIT. J. Synchrotron Radiat. 12, 537–541. http://dx.doi.org/10.1107/S0909049505012719.

Schmitt, C.N.Z., Politi, Y., Reinecke, A., Harrington, M.J., 2015. Role of sacrificial protein-metal bond exchange in mussel byssal thread self-healing. Biomacromolecules 16, 2852–2861. http://dx.doi.org/10.1021/acs.biomac.5b00803.

Schofield, R.M.S., 2003. Zinc is incorporated into cuticular "tools" after ecdysis: the time course of the zinc distribution in "tools" and whole bodies of an ant and a scorpion. J. Insect Physiol. 49, 31–44. http://dx.doi.org/10.1016/S0022-1910(02)00224-X.

Seto, J., Ma, Y., Davis, S.A., Meldrum, F.C., Gourrier, A., Kim, Y.-Y., Schilde, U., Sztucki, M., Burghammer, M., Maltsev, S., Jager, C., Colfen, H., 2012. Structure-property relationships of a biological mesocrystal in the adult sea urchin spine. Proc. Natl. Acad. Sci. 1–6. http://dx.doi.org/10.1073/pnas.1109243109.

Tan, Y., Hoon, S., Guerette, P.A., Wei, W., Ghadban, A., Hao, C., Miserez, A., Waite, J.H., 2015. Infiltration of chitin by protein coacervates defines the squid beak mechanical gradient. Nat. Chem. Biol. 11, 488–495. http://dx.doi.org/10.1038/nchembio.1833.

Tao, Y., Shokes, J., Scott, R.A., Nesson, M., Schofield, R.M.S., 2007. XAFS studies of transition metal and halogen biomaterials in invertebrate tools. In: X-Ray Absorption Fine Structure–XAFS13: 13th International Conference: Stanford, California, USA, 9–14 July, 2006. Amer Inst of Physics, p. 352.

White, S.R., Moore, J.S., Sottos, N.R., Krull, B.P., Santa Cruz, W. a, Gergely, R.C.R., 2014. Restoration of large damage volumes in polymers. Science 344, 620–623. http://dx.doi.org/10.1126/science.1251135.

Zubavichus, Y., Shaporenko, A., Grunze, M., Zharnikov, M., 2005. Innershell absorption spectroscopy of amino acids at all relevant absorption edges. J. Phys. Chem. A 109, 6998–7000. http://dx.doi.org/10.1021/jp0535846.